Superconductivity enhancement in phase-engineered molybdenum carbide/disulfide vertical heterostructures

Fu Zhang[a,b,1], Wenkai Zheng[c,d,1], Yanfu Lu[a,e,1], Lavish Pabbi[f], Kazunori Fujisawa[b,f,g], Ana Laura Elías[b,f], Anna R. Binion[f], Tomotaroh Granzier-Nakajima[b,f], Tianyi Zhang[a,b], Yu Lei[a,b], Zhong Lin[f], Eric W. Hudson[b,e,f], Susan B. Sinnott[a,b,e,h,2], Luis Balicas[c,d,2], and Mauricio Terrones[a,b,e,f,h,2]

[a]Department of Materials Science and Engineering, The Pennsylvania State University, University Park, PA 16802; [b]Center for 2-Dimensional and Layered Materials, The Pennsylvania State University, University Park, PA 16802; [c]National High Magnetic Field Laboratory, Florida State University, Tallahassee, FL 32310; [d]Department of Physics, Florida State University, Tallahassee, FL 32306; [e]Materials Research Institute, The Pennsylvania State University, University Park, PA 16802; [f]Department of Physics, The Pennsylvania State University, University Park, PA 16802; [g]Research Initiative for Supra-Materials, Shinshu University, 4-17-1 Wakasato, Nagano 380-8553, Japan; and [h]Department of Chemistry, The Pennsylvania State University, University Park, PA 16802

Stacking layers of atomically thin transition-metal carbides and two-dimensional (2D) semiconducting transition-metal dichalcogenides, could lead to nontrivial superconductivity and other unprecedented phenomena yet to be studied. In this work, superconducting α-phase thin molybdenum carbide flakes were first synthesized, and a subsequent sulfurization treatment induced the formation of vertical heterolayer systems consisting of different phases of molybdenum carbide—ranging from α to γ′ and γ phases—in conjunction with molybdenum sulfide layers. These transition-metal carbide/disulfide heterostructures exhibited critical superconducting temperatures as high as 6 K, higher than that of the starting single-phased α-Mo$_2$C (4 K). We analyzed possible interface configurations to explain the observed moiré patterns resulting from the vertical heterostacks. Our density-functional theory (DFT) calculations indicate that epitaxial strain and moiré patterns lead to a higher interfacial density of states, which favors superconductivity. Such engineered heterostructures might allow the coupling of superconductivity to the topologically nontrivial surface states featured by transition-metal carbide phases composing these heterostructures potentially leading to unconventional superconductivity. Moreover, we envisage that our approach could also be generalized to other metal carbide and nitride systems that could exhibit high-temperature superconductivity.

superconductivity | heterostructure | molybdenum carbide | molybdenum disulfide

High-quality layered crystals beyond graphene exhibit new physics inherent to the emerging functionalities made possible by thinning them down to the atomic limit. Particularly, two-dimensional (2D) materials are excellent candidates that serve as platforms for energy storage catalysts, and electronics/optoelectronics components (1, 2). More exotic physical phenomena, such as superconductivity, have also been reported in atomically thin systems (3–5). Interestingly, superconductivity is found to exhibit unique properties in the 2D limit. For example, monolayer FeSe grown on SrTiO$_3$ displays superconductivity at temperatures as high as $T_C \cong 100$ K (3), in contrast to its bulk value $T_C \cong 8$ K. Similarly, ionic liquid-induced superconductivity on the surface of semiconducting transition-metal dichalcogenides (4) (TMDs), such as MoS$_2$, as well as the intrinsic superconductivity in exfoliated metallic TMDs (e.g., NbSe$_2$) display a remarkable resilience against external magnetic fields applied along a planar direction (5–7). This has been assumed to be evidence for the so-called Ising-paired state, whose spin-singlet Cooper pairing would occur among carriers at the K and K' valleys having opposite spins. Moreover, in 2D MoTe$_2$, a type-II Weyl semimetal, T_C can be enhanced either through a sulfur doping driven phase transition (from the monoclinic 1T′ to the orthorhombic T$_d$ phase) (8), which is claimed to enhance the electron–phonon coupling (9), or through exfoliation down to

the monolayer limit (10). Two-dimensional superconductivity is now emerging as a scientific frontier addressing a number of unanswered questions, such as the disparate evolution of the superconducting transition temperature as a function of the number of layers and different stackings within different compounds (6, 7).

Nearly 2D α-phase Mo$_2$C crystals, have been recently synthesized via chemical vapor deposition (CVD). As-grown high quality 2D α-Mo$_2$C displays a thickness dependent superconducting transition temperature (T_C) up to 4 K (11). Therefore, transition metal carbides (TMCs) stand as an attractive platform for studying the intrinsic properties of superconductivity in two dimensions (11). It is interesting to notice that the different phases of molybdenum carbide, including α, β, and γ phases, were recently predicted to display topologically nontrivial electronic bulk bands that would lead to unconventional topological surface states (12, 13). These bulk and related surface states could be harvested to induce unconventional, and hopefully topological, superconductivity through the proximity effect (14) with a superconductor such as α-phase Mo$_2$C.

> **Significance**
>
> We demonstrate that engineering of two-dimensional molybdenum carbide/disulfide heterostructures can result in superconducting architectures with higher critical temperatures than that of pristine α-Mo$_2$C. We developed a gas-phase reaction approach for the heterostack formation via phase transitions, which involves short sulfurization times (1–5 min) of α-Mo$_2$C films. Heterostructures of α-Mo$_2$C and γ′-phase MoC$_{1-x}$ exhibit superconductivity with a higher critical temperature ($T_C \sim 6.8$ K) than the original Mo$_2$C crystal ($T_C \sim 4.0$ K). The distinct chemical composition and modified structure of the metastable γ′-MoC$_{1-x}$ phase present in the layered structure might lead to a higher interfacial density of states and increase in the frequency of the relevant phonon modes, thus contributing to the superconductivity and hence to a higher T_C.

APPLIED PHYSICAL SCIENCES

Multiple phases have been observed in molybdenum carbide, as identified through their crystallographic structures (orthorhombic α-phase, hexagonal η-phase, and cubic δ-phase), their Mo:C composition ratios (α-Mo_2C, γ′-MoC_{1-x}, γ-MoC, and η-MoC), and by the observed order or disorder related to interstitial carbon atoms within the molybdenum metal matrix (α- and β-phase Mo_2C) (15). The different phases display distinct properties that could lead to the manipulation of the superconductivity in carbide systems via phase transitions and through the fabrication of vertical carbide/disulfide heterostructures with several epitaxial relationships, including strained phases and moiré engineering using different stacking rotation angles. Multilayer $W_xMo_{1-x}C_yS_2$ has already been synthesized through oxidation and sulfurization of mixtures of Mo and WC at high temperatures (800–1,100 °C) by Terrones and coworkers, in 2000 (16). Consequently, these multilayer systems offer the possibility of tuning their superconductivity properties via sulfur incorporation.

In this work, we report the synthesis of molybdenum carbide/disulfide vertical heterostructures through a two-step approach, involving the CVD growth of thin α-Mo_2C crystals, followed by low-pressure sulfurization at high temperature (see *Materials and Methods* and *SI Appendix*, Figs. S1 and S2 for details) (11). The obtained morphologies for the initial α-Mo_2C flakes are shown in a representative scanning electron microscopy (SEM) image (Fig. 1 *A*, *Inset*) and in the optical image shown in *SI Appendix, Fig. 1A*. The synthesized α-Mo_2C thin crystals exhibit different faceted shapes (frequently hexagonal) with typical lateral sizes of around 20 µm. X-ray diffraction (XRD) studies were conducted to identify the phase and orientation of the synthesized material (Fig. 1*C*), which was confirmed to be α-Mo_2C, and corresponding to an orthorhombic crystalline lattice with the Mo atoms positioned in a slightly distorted hexagonal close-packed arrangement (Fig. 2*E*). The α-Mo_2C thin crystals preferentially grew vertical to the (200) direction (corresponding to the XRD peak at 38.1°). In addition, the small diffraction shoulder peak next to the (200) planes and the small reflection located at 47.8° in the pattern correspond to the (001) and (201) orientations of α-Mo_2C, respectively (17). X-ray photoelectron spectroscopy (XPS) analyses were used to further investigate the chemical composition, bonding environment, and valence states of the synthesized materials. The Mo 3d line scan of pristine α-Mo_2C shown in Fig. 1*G* is dominated by molybdenum carbide (MoC_x), oxide (MoO_3 at 232.5 and 235.6 eV; MoO_2 at 229.1 and 232.3 eV), and oxycarbide (MoO_xC_y) signals (18). Doublets of MoO_3 (Mo^{6+}) and MoO_2 (Mo^{4+}) can be observed due to surface oxidation. The doublets appear at 228.0 and 231.1 eV, corresponding to Mo^{2+} $3d_{5/2}$ and Mo^{2+} $3d_{3/2}$ of α-Mo_2C, respectively (19).

The crystalline structure of the as-grown Mo_2C was also confirmed to correspond to α-phase by atomic resolution scanning tunneling microscopy (STM, Fig. 1*A*), transmission electron microscopy (TEM; *SI Appendix*, Fig. S1), high-angle annular dark-field scanning TEM (HAADF-STEM; Fig. 2*E*) and selected area diffraction patterns (SAED; Fig. 2*I* and *SI Appendix*, Fig. S1*C*). The ordered carbons that fill the distorted hexagonal metal matrix voids (20), are responsible for the formation of superlattices (21) (associated Bragg peaks are indicated by the red arrows in Fig. 2*I* and *SI Appendix*, Fig. S1*C*). *SI Appendix, Fig. S1E* shows a TEM planar view of the atomic registry of Mo_2C displaying hexagonal patterns with a Mo-Mo distance of ∼0.23 nm, which agrees well with the representative STM image shown in Fig. 1*A*. TEM analyses in both planar and cross-sectional directions of pristine α-Mo_2C are also demonstrated in *SI Appendix, Figs. S1, S3, and S4*. Electron energy-loss spectroscopy (EELS) and additional SAED patterns can be found in *SI Appendix, Fig. S3*, all in good agreement with the determined α-Mo_2C phase.

Interestingly, the synthesized molybdenum carbide/disulfide heterostacks (Fig. 1*B*) constitute superlattices with well-defined moiré patterns with a moiré lattice constant of around 2.8 nm, as identified by atomic resolution STM. Fig. 1*B* exhibits a lattice

overlap between MoS_2 and γ-phase MoC at a 0° stacking angle (*SI Appendix*, Fig. S5). XRD analyses (Fig. 1*D*) confirm the 2H-MoS_2 formation [the 14.1° peak in Fig. 1*D* corresponds to the (002) plane of MoS_2], and provide evidence for a phase transition experienced by the molybdenum carbide. We note that the original Mo_2C in the α-phase (orthorhombic) is partially transformed to the γ-phase of MoC (hexagonal, with an AAAA stacking sequence of metal planes with carbon in the octahedral sites), as indicated by the high-intensity reflection located at 2θ = 33.0°, which corresponds to the (001) plane of γ-MoC. The α-Mo_2C and γ-MoC are the only two thermodynamically stable phases of molybdenum carbide at room temperature, according to the Mo-C phase-diagram (22). However, the formation of a ternary molybdenum–carbon–sulfur alloy may stabilize an intermediate metastable carbide phase, γ′-phase MoC_{1-x} (15). Similar to the γ-MoC phase, the substoichiometric γ′-MoC_{1-x} phase also crystallizes in a hexagonal structure but with a slightly different stacking order in the Mo matrix and distinct carbon occupancies (hexagonal, AABB stacking sequence) (23). γ-MoC and γ′-MoC_{1-x} are virtually indistinguishable by XRD. It is noteworthy that such a phase transition does not occur through a simple annealing of the α-Mo_2C phase at high temperature (XRD shown in *SI Appendix*, Fig. S6). However, MoC (or MoC_{1-x}) could be present in small quantities in pristine α-Mo_2C due to the presence of stacking faults originating from Mo deficiency, as concluded from the small intensity (001) reflection that can be observed in the Fig. 1*C* XRD pattern. It is believed that sulfur incorporation can induce the formation of ternary solid solutions of Mo-C-S, while internal local strain and an excess of sulfur would trigger phase segregation between the carbide and the disulfide. Sulfur will consequently extract the Mo atoms from α-Mo_2C, thus leading to the Mo:C atomic ratio gradually decreasing from 2:1–1:1, and resulting in the consecutive α to γ′ to γ phase transitions, responsible for ultimately forming the γ-MoC/MoS_2 vertical heterostructures for longer sulfurization treatments. The MoC_{1-x} phase (γ′) was reported to display higher Debye temperatures and stronger electron-phonon coupling when compared to the α-Mo_2C phase, which could lead to higher superconducting transition temperatures (24, 25). In fact, an increase in T_C is indeed observed in the heterostructure upon sulfur incorporation, as described by the detailed measurements shown below.

XPS analysis carried out in molybdenum carbide/disulfide vertical heterostructures (Fig. 1*H*) revealed peaks corresponding to binding energies of molybdenum oxides (MoO_2 and MoO_3). Molybdenum carbide is beyond the XPS detection depth as it lays under MoS_2 layers, thus MoC_x doublets are not detected in the line scans. Additionally, the spectrum displays a small bump located at 226.4 eV, which is associated with elemental S in the 2s region after a short sulfurization time (5 min). Moreover, the Mo 3d line scan reveals the presence of the doublet peaks at 228.7 and 232.0 eV (Fig. 1*H*), which correspond to the Mo^{4+} $3d_{5/2}$ and Mo^{4+} $3d_{3/2}$ binding energies of MoS_2, respectively. The doublet observed at 162.0- and 163.2-eV peaks is found in the S 2p line scan (*SI Appendix*, Fig. S7), corresponding to $2p_{3/2}$ and $2p_{1/2}$, respectively. Their energy separation is ∼1.2 eV, which is consistent with the fingerprint of S^{2-} in MoS_2 (18). Raman spectra demonstrate the emergence of the two main peaks identified as the 2H-MoS_2 E_{2g}^1 and the A_{1g} phonon modes, after sulfurization of α-Mo_2C (Fig. 1 *E* and *F*). The difference in frequency between these two phonon modes is Δk ∼23 cm^{-1} in the spectra corresponding to a heterostructure resulting from a 5-min sulfurization treatment, thus indicating the presence of few layers MoS_2 (26). Cross-sectional TEM confirms the presence of a few layers MoS_2 on the surface of the sample after sulfurized for 5 min (Fig. 2*G*).

Sulfurization treatments performed on thin α-Mo_2C during various times lead to vertical heterostructures with different crystallographic correspondences between the carbides and the
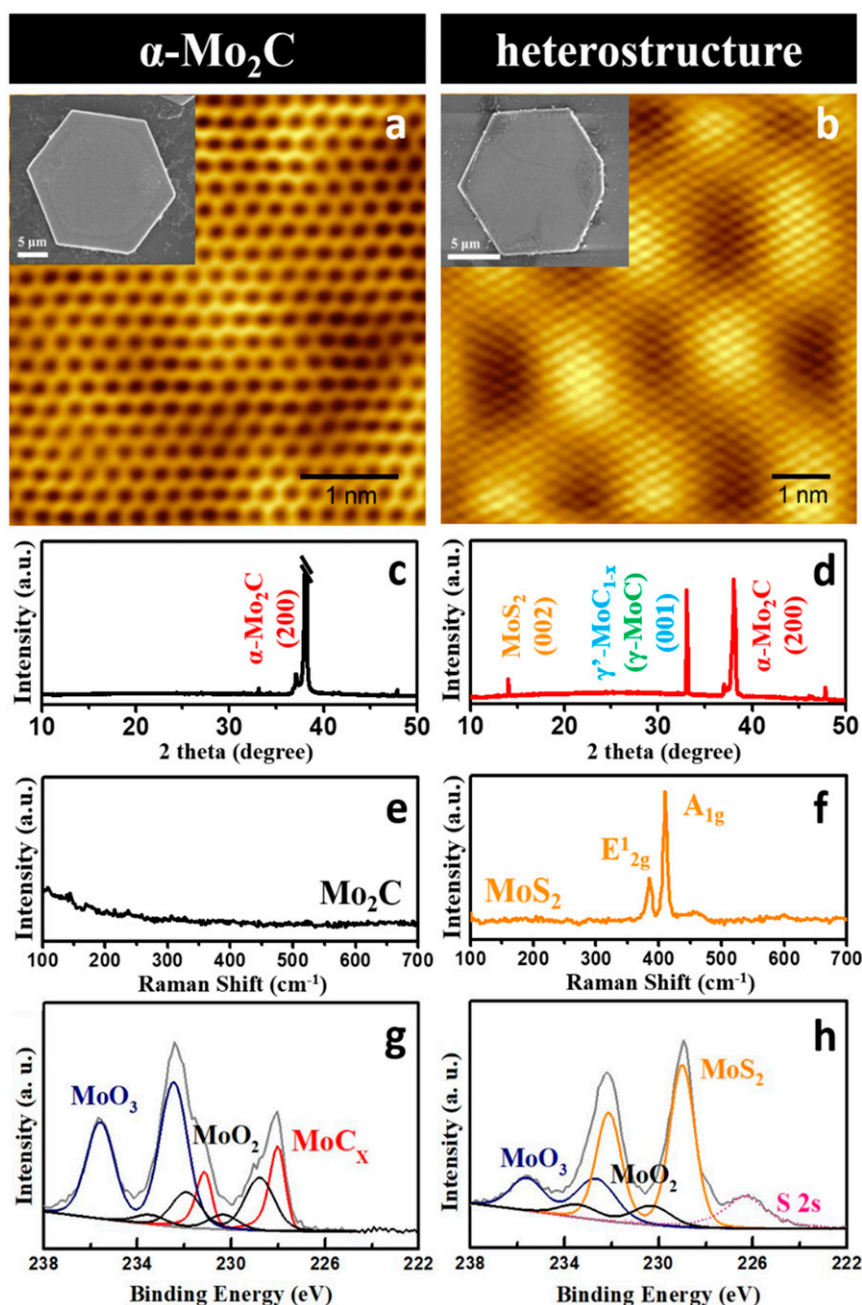
Fig. 1. Characterization of α-Mo$_2$C and molybdenum carbide/disulfide heterostructures. (*A*) STM images of crystals as-grown α-Mo$_2$C (*Insets* depict SEM); (*B*), a molybdenum carbide/disulfide heterostack obtained after a 5-min H$_2$S treatment of Mo$_2$C; (*C* and *D*) XRD patterns and (*E* and *F*) Raman spectra of pristine Mo$_2$C and a molybdenum carbide/disulfide heterostructure on Si/SiO$_2$, respectively; (*G* and *H*) Representative XPS Mo 3d high-resolution line scans obtained from the structures depicted in *A* and *B*, respectively.

sulfide. Schematic representations of the observed crystallographic phases and the corresponding cross-sectional TEM images of pristine α-Mo$_2$C and of the various synthesized heterostructures (obtained after 1-, 5-, and 20-min sulfurization treatments) are depicted in Fig. 2. It is noted that the cross-sectional TEM samples of as-synthesized pristine α-Mo$_2$C and heterostructures were prepared by SEM focused ion beam (FIB) from the same flakes integrated in transport devices (see transport measurement discussion below). The α-Mo$_2$C HAADF-STEM images display an atomically flat surface with an interlayer spacing of ∼0.23 nm (Fig. 2*E*, and *SI Appendix*, Fig. 1 *B* and *D*). High-resolution TEM images revealed the presence of the metastable γ′-MoC$_{1−x}$ stacked together with α-Mo$_2$C (Fig. 2 *B* and *F*).

γ′-MoC$_{1−x}$ is possibly stabilized by a thin layer of sulfur. The carbide surface was found to be covered by thin layers of MoS$_2$ after a 5-min sulfurization treatment (Fig. 2 *C* and *G*), exhibiting a mixture of γ′(γ)- and α-phases underneath. The stacking between MoS$_2$ and γ-MoC creates the moiré pattern exhibited in Fig. 1*B*. Elemental energy-dispersive spectroscopy (EDS) mapping results of the cross-sectional interface were acquired slice-by-slice, providing compositional information (*SI Appendix*, Fig. S8). The elemental mappings clearly revealed that the Mo:C ratio gradually decreases from 2:1–1:1 while moving toward the side of the carbide exposed to sulfur, indicating that the molybdenum atoms paired up with sulfur to form layers of MoS$_2$, thus the carbide phase transition could have been directly induced by
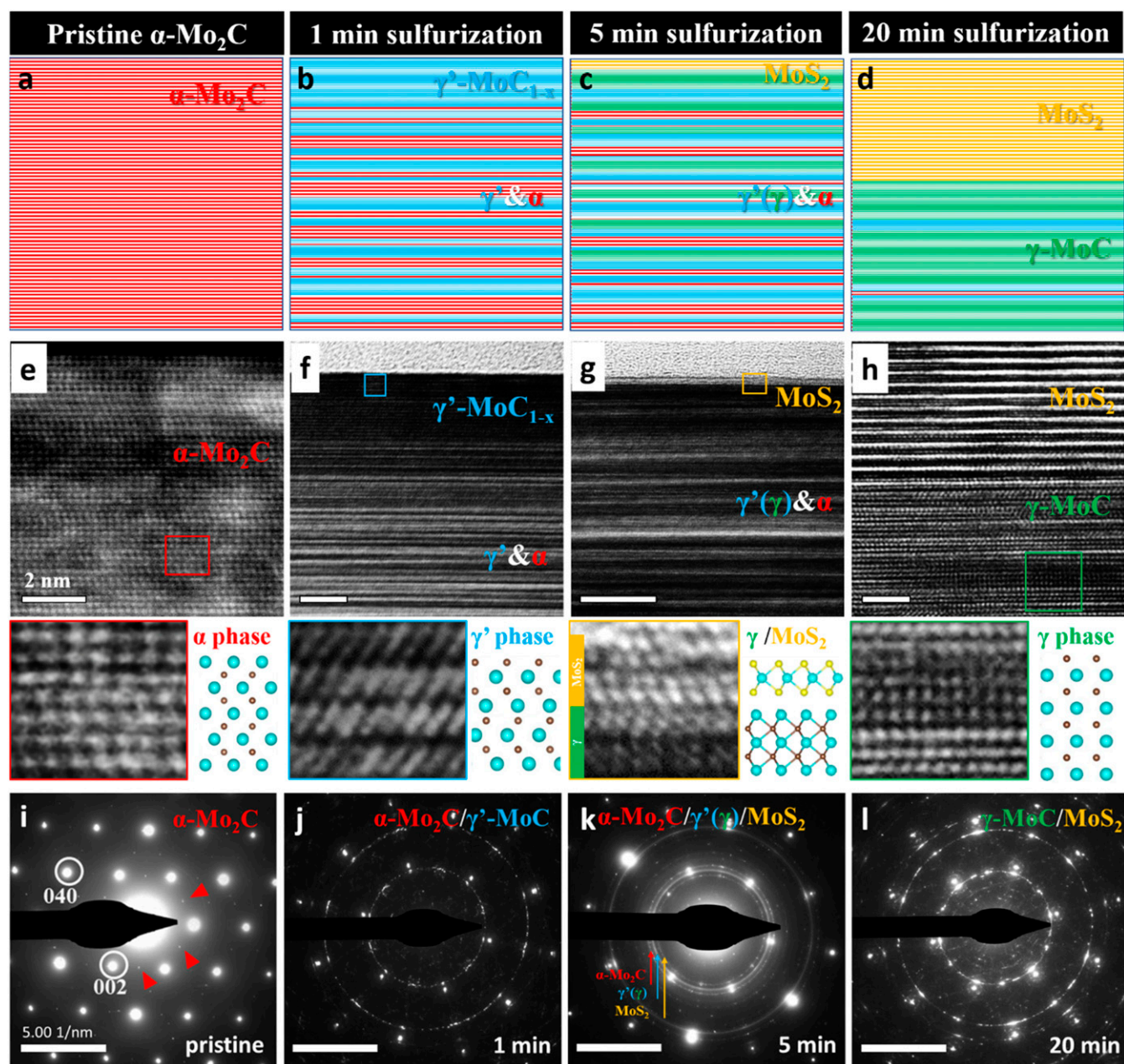
Fig. 2. TEM analyses of the phase evolution in molybdenum carbide/disulfide heterostack. (*A–D*) Schematic views of the crystallographic phases identified in the cross-sectional TEM views of α-Mo$_2$C (*A*) and molybdenum carbide/disulfide heterostructures [after 1-min (*B*); 5-min (*C*); and 20-min (*D*) sulfurization treatments]. (*E*) Cross-sectional HAADF-STEM images of pristine Mo$_2$C and (*F* and *H*) HRTEM images of molybdenum carbide/disulfide heterostacks after 1-, 5-, and 20-min sulfurization, respectively; atomic-resolution TEM images reveal the phase transitions induced by the sulfurization process (*Insets*). Planar-view SAED analyses of pristine Mo$_2$C (*I*) and molybdenum carbide/disulfide heterostructures for H$_2$S reaction times of 1 min (*J*), 5 min (*K*), and 20 min (*L*).

chalcogen incorporation in the system. Density-functional theory (DFT) calculations were performed to obtain the formation energies of various MoC$_{1-x}$ compositions resulting by adding C interstitials in α-Mo$_2$C and by creating C vacancies in γ-MoC. The results indicate that a relatively low activation energy is needed to overcome the energy barrier required to add C interstitials to α-Mo$_2$C (*SI Appendix*, Fig. S9). High-resolution (HRTEM) images of samples obtained after 20 min of H$_2$S treatment display 10–15 layers of MoS$_2$ forming a heterostructure with γ-MoC (Fig. 2*D*, *H*, and *L* and zoom-out regions in *SI Appendix*, Fig. S10). Therefore, we can conclude that the thickness of the MoS$_2$ layers is directly correlated to the H$_2$S treatment time. Moreover, the disulfide formation does not only happen on the basal

plane of the carbide, but it is also selectively formed through stacking faults at edge sites (*SI Appendix*, Fig. S11) (27). Such hybrid stacks hold a great promise as catalysts for energy conversion and as Josephson junction assemblies (28).

The planar-view TEM/SAED patterns of the molybdenum carbide/disulfide stacks as a function of sulfurization time are displayed in Fig. 2 *I–L*. A series of shifts can be found in the diffraction patterns upon sulfurization, indicating that the α-Mo$_2$C phase (red) undergoes a phase transition toward the γ'-MoC$_{1-x}$ phase (blue) and/or γ-MoC phase (green). Such SAED patterns exhibit hexagonal rings on the plane perpendicular to the [001] zone axis (indicated by the yellow arrow in Fig. 2*K*), which result from the formation of a polycrystalline thin film of MoS$_2$. Moreover,

the diffraction pattern reveals that a large portion of the MoS_2 film displays a preferred orientation with a nearly 0° misorientation with respect to γ-MoC, thus confirming the epitaxial growth of MoS_2 on the underlying hexagonal γ-MoC. A proposed evolution model for chalcogen incorporation in 2D molybdenum carbide is discussed in *SI Appendix*, Fig. S12.

Various possible epitaxial configurations for heterostructures confining MoS_2 inside MoC layers were studied using DFT calculations. The interfacial structure between γ-MoC and MoS_2 is predicted to be in two possible stable configurations. In one of them, the MoS_2 could be confined under compressive epitaxial strain in the γ-MoC/MoS_2/γ-MoC sandwich structure illustrated in Fig. 3 *A* and *E*, that is in a strained-epitaxial state. In the second configuration, the MoS_2 would form a moiré pattern with γ-MoC, as a result of van der Waals (vdW) epitaxy, as shown in Fig. 3*I*. To discover the vertical heterostructure with the lowest relative formation energy, different interfacial terminations of γ-MoC were analyzed. For the strained-epitaxial vertical heterostructure, since the space group of both MoS_2 and γ-MoC is $P\bar{6}m2$ the hexagonal ring of S atoms in the MoS_2 will overlap with the hexagonal ring of either Mo or C atoms in the γ-MoC. Based on the equation the formation energy of the Mo-terminated structure was found to be −0.01 eV/atom, while the formation energy of the C-terminated structure was +0.19 eV per atom. Therefore, the Mo-terminated structure was considered for the strained-epitaxial heterostructure (*SI Appendix*, Table S1). For the moiré heterostructure, the same equation gives a formation energy of +0.01 eV/atom for the C-terminated structure (*SI Appendix*, Table S1), which is predicted to be more stable than the Mo-terminated case (which has an E_f = +0.22 eV per atom). Therefore, both crystallographic correspondences may coexist based on the stability of the overall structure when the number of MoS_2 and γ-MoC layers are the same, which is confirmed by TEM observations (Fig. 3 *E* and *F*). The side views of both possible vertical heterostructures are overlapped with the HRTEM images in Fig. 3 *D–F*. The work of adhesion of the strained-epitaxial and moiré heterostructures was derived by adding a 20-Å vacuum layer at the interface and, subsequently, calculating the energy difference between the structures with and without vacuum, thus yielding a work of adhesion of 2.17 and 0.56 J/m², respectively.

The phase-transition-induced strain at the molybdenum carbide/disulfide interfaces drastically modifies the electronic properties of the semiconducting MoS_2, as predicted by DFT calculations. The density of states (DOS) at the interfaces was analyzed to quantify

changes corresponding to each atomic layer in the direction perpendicular to the interface, to calculate the bandgap of each MoS_2 layer, and determine the electronic contributions to the adjustment of bandgaps (Fig. 4 *A–C*). In the strained-epitaxial vertical heterostructure, when one layer of MoS_2 and six layers of MoC were stacked (Figs. 3 *A* and *D* and 4*A*), the MoS_2 underwent a −6.5% change in epitaxial strain with a bandgap of 0.25 eV, which represents a 1.44-eV reduction when compared to the bandgap of a relaxed MoS_2 monolayer. A comparison between the DFT-calculated DOS and the experimental d*I*/d*V* curve obtained by scanning tunneling spectroscopy measurements on a carbide/disulfide heterostructure (5-min sulfurized) displays an excellent match in the 250-meV bandgap of strained-epitaxial MoS_2 embedded in MoC (1MoS_2 with 6MoC) (*SI Appendix*, Fig. S13). The calculated DOS predicts that the Mo d orbitals in the two layers of γ-MoC closest to the interface were altered the most. The main contribution to the bandgap changes in monolayered MoS_2 is likely coming from its relatively large epitaxial strain, which influences the d orbital of Mo in both MoS_2 and γ-MoC, and the p orbital of S in the MoS_2. When three layers of MoS_2 and six metal layers of MoC were stacked (Figs. 3*B* and *E* and 4*B*), the MoS_2 layers were under a −5.7% epitaxial strain, and the bandgaps of the interfacial layer and middle layer were 0.81 and 1.12 eV, respectively. In this case, there is no vdW interface between the MoS_2 and γ-MoC layers, thus the d orbitals of Mo in the interfacial layer and the middle layer of MoS_2 were different in both the valence and the conduction bands within the DOS. In addition, the d orbitals of Mo in the first and second interfacial layers of γ-MoC were dramatically different from one another. Based on a comparison between one layer versus three layers of MoS_2 at the epitaxially strained interface, the calculations indicate that if more layers of MoS_2 were stacked, the middle layers would behave like bulk MoS_2 without strain confinement. In contrast, for the moiré heterostructures (Figs. 3 *C* and *F* and 4*C*), the bandgaps of the interfacial and middle layers were very close to the reported bandgap for three layers of MoS_2 (1.35 and 1.39 eV, respectively) (29). Because of the weak vdW interaction at the interface, the changes of the Mo d orbitals in both MoS_2 and γ-MoC were much less than in the case of the strained-epitaxial heterostructure. Furthermore, the differences in atomic interactions at the interface have been demonstrated in the electron density maps (Fig. 4 *A–C*). In the three-layer MoS_2 strained-epitaxial heterostructure (Fig. 3 *B*, *E*, and *H*), the contrasting electron densities at both the interface and between the MoS_2 layers indicate that the atomic interaction at the interfaces is not
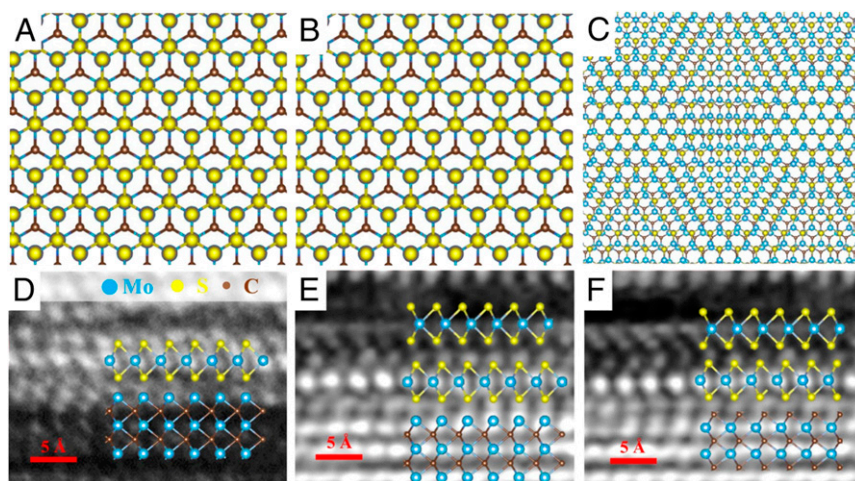
Fig. 3. Different molybdenum carbide/disulfide heterostructures. Planar schematic view of the (*A*) one-layer MoS_2 and γ-MoC heterostructure in a strained-epitaxial state, (*B*) three-layer MoS_2 sandwiched by γ-MoC in a strained-epitaxial state, and (*C*) three-layer MoS_2 sandwiched by γ-MoC, forming a moiré superlattice. (*D–F*) Schematic side views of the heterostructures in *A–C* overlapped with the TEM images, respectively.
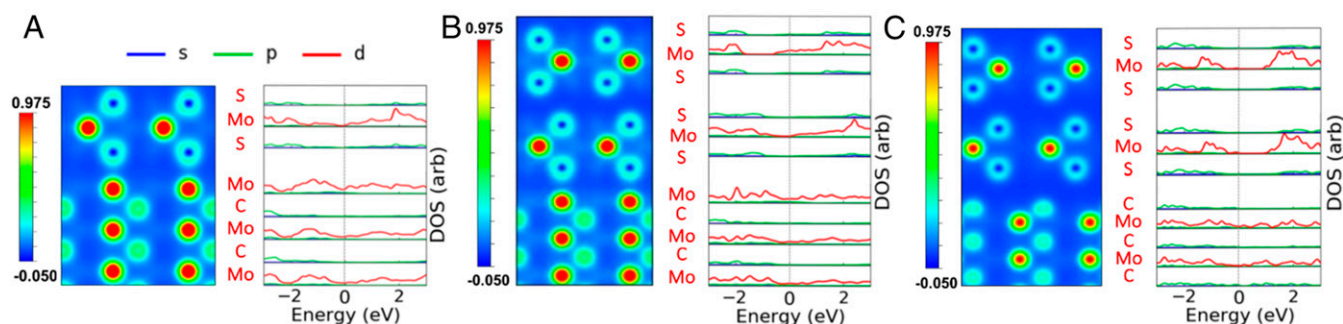
Fig. 4. Electronic properties of different molybdenum carbide/disulfide heterostructures. Electron density map (scale units 10^2 e/Å^3) and DOS in s, p, and d orbitals at each atomic layer corresponding to the side-view crystal structures illustrated in Fig. 3 *D–F*, respectively. The types of elements are indicated in red in each atomic layer. (*A*) One-layer MoS$_2$ and γ-MoC in a strained-epitaxial state. (*B*) Three-layer MoS$_2$ sandwiched by γ-MoC in a strained-epitaxial state. (*C*) Three-layer MoS$_2$ sandwiched by γ-MoC, forming a moiré superlattice. Notice the increase of the DOS at the interphase between molybdenum sulfide and carbide for the strained-epitaxial configuration.

vdW-like, which confirms the trend noted in the work of adhesion. The higher electron density and work of adhesion in strained-epitaxial heterostructures indicate that the interatomic dispersion is much stronger than the vdW interaction and slightly weaker than the Mo–S covalent bond in MoS$_2$. In contrast, for moiré heterostructures, the comparable electron densities at the γ-MoC interface and between the MoS$_2$ layers indicate that the atomic interaction is comparable to the vdW interaction between the MoS$_2$ layers.

We studied the transport properties of pristine α-Mo$_2$C, chosen as reference, and of the molybdenum carbide/disulfide heterostructure in order to detect superconductivity in the latter (measurement scheme is depicted in *SI Appendix*, Fig. S14). As previously mentioned, the flakes used for transport measurement correspond to the same flakes analyzed in the cross-sectional TEM images discussed above (Fig. 2). Fig. 5*A* shows the resistivity as a function of temperature for a 60-nm-thick pristine α-Mo$_2$C crystal. The inset clearly indicates that the sample becomes superconducting at $T_C \cong 4$ K, as previously reported (11). The finite resistivity observed below T_C results from the physical or electrical connection between the α-Mo$_2$C crystal and, possibly, the graphene layer formed during the synthesis process (*SI Appendix*, Fig. 3). As seen, the transition is very sharp, displaying a width of less than 0.2 K. This, combined with the low residual resistivity ρ (4 K) ∼ 1 μΩ cm and the large residual resistivity ratio ρ (300 K)/ρ (4 K) = 22, indicates a high-quality single crystal. Fig. 5 *B* and *C* display ρ as a function of *T* for two samples sulfurized for 5 and 20 min, respectively. The onset of the resistive transition for the sample sulfurized for 5 min (thickness ∼40 nm) is $T \cong 6$ K, which is 50% higher than the onset of the superconducting transition for pristine α-Mo$_2$C. As seen in the inset of Fig. 5*B*, the resistive transition reveals multiple steps, indicating an inhomogeneous material, or the coexistence of multiple crystallographic phases. The lowest resistive step occurs at around 4 K, which corresponds to the T_C of pristine α-Mo$_2$C. Based on our structural analysis we argue that the observation of a higher T_C is associated with the γ′-MoC$_{1-x}$ phase. Fig. 5*C* shows the resistivity as a function of temperature for a 40-nm-thick MoS$_2$/γ-MoC heterostructure resulting from a 20-min sulfurization process. The heterostructure clearly displays a metallic behavior over the entire temperature range, although no superconductivity is observed down to $T = 1.8$ K, as expected for γ-MoC. The incorporation of the MoS$_2$ layer leads to a rather high residual resistivity. Given that most of the current should be carried by the γ-MoC layers sandwiched between the MoS$_2$ layers, such a high residual resistivity would point to either a significant density of defects in the γ-MoC layers, or to a low density of carriers, or to both in addition to an effective cross-sectional area smaller than the thickness used to calculate the

resistivity. Detailed analysis of the 1-min sulfurized sample is discussed in *SI Appendix*, Fig. S15; no sulfide formation is observed from SAED (Fig. 2*F*) and Raman analyses. Interestingly, the onset of the resistance reduction for 1-min sulfurized sample (thickness ∼50 nm) is $T \cong 6.8$ K, which is 70% higher than that of the superconducting transition for pristine α-Mo$_2$C. We attribute such T_C enhancement in the 1-min sulfurized sample to the strain induced between alternating layers of γ′-MoC$_{1-x}$ and α-Mo$_2$C, originated by the S diffusion along cracking faults of α-Mo$_2$C (Fig. 2 *B*, *F*, and *J*). There is, however, a nonzero residual resistance, which could well be related to the presence of graphene layers deposited during the α-Mo$_2$C growth. We should point out that further studies on the short time sulfurization processes (1–2 min) that result in stacked layers of γ′-MoC$_{1-x}$ and α-Mo$_2$C (not sulfides) are currently underway but these are out of the scope of this paper related to vertical heterostacks of carbides and sulfides.

Fig. 5 *D* and *E* display the resistivity as a function of the magnetic field μ$_0$H at various constant temperatures, unveiling the superconducting to metallic phase transitions for fields oriented perpendicularly to the planes of pristine α-Mo$_2$C and γ′-MoC$_{1-x}$, respectively. The insets in both figures display the upper critical field H_{c2}^c for fields along the *c* axis as a function of the temperature, where red lines are linear fits. Here, to define the value of H_{c2}^c we chose the 90% criteria or the field value where the resistivity reaches 90% of its value in the normal state just above the transition. The linear temperature behavior is consistent with the 2D Ginzburg–Landau formalism for fields perpendicular to the planes: $\mu_0 H_{c2}^c = \Phi_0(1 - T/T_C)/2\pi\xi_{ab}^2$, where Φ_0 is the magnetic flux quantum, μ$_0$ the permeability of free space, and ξ_{ab} is the in-plane coherence length. This supports the 2D nature of the superconducting state in these crystals despite their sizable thicknesses.

Fig. 5*F* displays the isothermal ρ for the sample sulfurized for 20 min as a function of μ$_0$H. A negative magnetoresistivity is observed for μ$_0$H < 1 T and for all temperatures, which we tentatively attribute to weak antilocalization (30). An oscillatory signal, which can be suppressed by increasing the temperature, emerges when μ$_0$H > 5 T. These oscillations turn out to be periodic in inverse fields, indicating that these would correspond to Shubnikov–de Haas oscillations. The inset reveals the oscillatory component once the background magnetoresistivity is subtracted through a polynomial fit. The observation of quantum oscillations is rather surprising given the very large residual resistivity observed in the MoS$_2$/γ-MoC heterostructure, and suggests that small regions of the γ-MoC should be well-ordered from a crystallographic perspective. It is important to note that the residual resistivity and Tc of the samples synthesized at 1 and 5 min could be tuned as a function of the lateral crystal uniformity of the samples, if careful thermal annealing after sulfurization takes
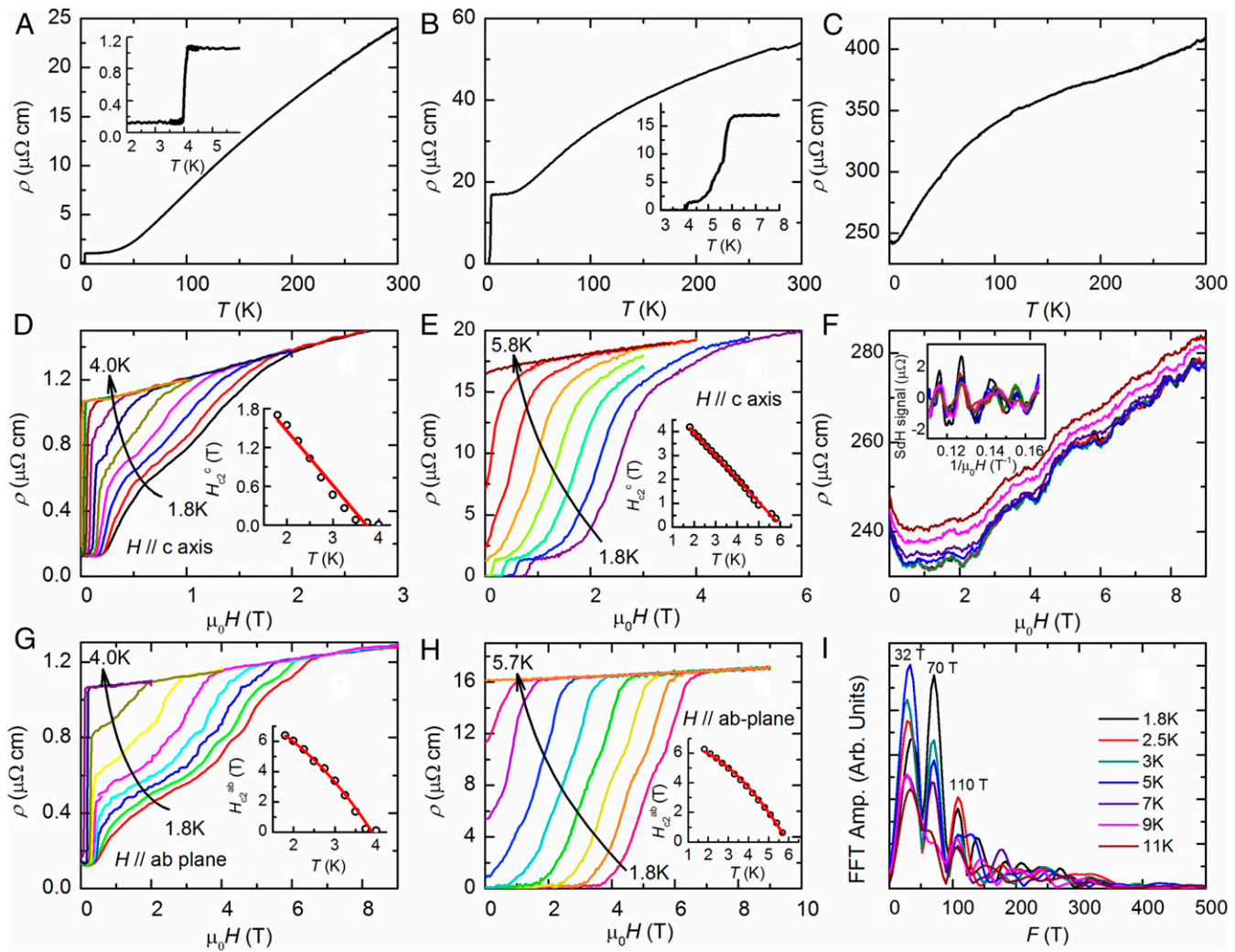
Fig. 5. Evolution of the superconducting state in molybdenum carbide/disulfide vertical heterostructures subjected to different sulfurization times. (*A–C*) Resistivity ρ as a function of the temperature *T* for pristine α-Mo$_2$C (*A*) and for molybdenum carbide/disulfide heterostructures subjected to 5 min (*B*), and 20-min (*C*) sulfurization. Insets in a and b display ρ as a function of *T* in the low-temperature region where the superconducting transitions, starting at $T_C = 4$ and 6 K, respectively, become clearly visible. (*D–F*) ρ as a function of the external magnetic field μ$_0$H applied along the interlayer *c* axis for pristine α-Mo$_2$C (*D*) and heterostructures after a 5-min (*E*) and 20-min (*F*) sulfurization, and for several temperatures. (*D* and *E, Insets*) The upper-critical fields H_{c2}^c for fields along the *c* axis as a function of *T*, where red lines are fits to the conventional GL expression. (*F, Inset*) The Shubnikov–de Haas (SdH) signal after subtraction of a background polynomial. (*G–H*) Same as in *D* and *E* but for fields along the *ab* plane. (*G* and *H, Insets*) H_{c2}^{ab} for μ$_0$H//ab plane as a function of *T*. Notice the marked anisotropy between fields along the *ab* plane and along the *c* axis. (*I*) Fast Fourier transform of the oscillatory signal superimposed onto the magnetoresistivity of the MoS$_2$/γ-MoC heterostructure, exhibiting three main peaks at frequencies $F_\alpha \cong 30$ T, $F_\beta \cong 70$ T, and $F_\gamma \cong 110$ T.

place. This will require another in-depth study, involving different sulfurization times at various temperatures, transport measurements of all these phases in addition to TEM cross-sectional studies and structural characterization, and is beyond the scope of the current paper. It is noteworthy that as the sulfurization time increases, the fraction of semiconducting MoS$_2$ layers increases, thus altering the residual resistivity values. Therefore, the regime where three or four phases of layered carbides and sulfides coexist shows remarkable transport properties and should be studied for other analog systems.

Fig. 5 *G* and *H* display the temperature dependence of the resistive transition for fields along the conducting planes. There is anisotropy in upper-critical fields between both field orientations (by comparing with Fig. 5*D* and 5*E*, respectively), and the superconducting transition is inhomogeneous. This inhomogeneity probably results from a combination of vortex physics, crystallographic heterogeneity, or variations in composition. In

both panels, the insets show the upper-critical fields as a function of temperature, which is consistent with the conventional Ginzburg–Landau (GL) behavior. Red lines are fits to the conventional GL expression:

$$H_{c2}^{ab}(T) = \Phi_0 \left(1 - \left(\frac{T}{T_C}\right)^2\right) \Big/ 2\pi \xi_{ab}\xi_c,　　[1]$$

where ξ_c is the interplanar coherence length. The good fit to a conventional three-dimensional (3D) GL expression contradicts the behavior observed for fields applied perpendicularly to the planes that, instead, suggests 2D superconductivity. The 2D GL formalism predicts a $T^{1/2}$ dependence for H_{c2}^{ab} near T_C. One way to reconcile both observations is to assume that one is in an intermediate regime, approaching the 2D superconducting limit, but still in a 3D regime due to the thicknesses of these crystals, which are multilayered.

Finally, Fig. 5*I* displays the Fourier transform of the oscillatory signal shown in the inset of Fig. 5*F*. Two main frequencies *F* are observable in the range up to 400 T, $F_\alpha = 30$ T, $F_\beta = 70$ T, and $F\gamma = 110$ T, respectively. Such peaks indicate that the observed oscillations correspond to the Shubnikov–de Haas effect resulting from the Landau quantization of the electronic orbits. These small frequencies indicate small Fermi surface extremal cross-sectional areas (31). These oscillations are observable up to high temperatures, indicating light effective masses (32) as seen in semimetallic systems. Indeed, through the Lifshitz–Kosevich formalism, we extract fairly light effective masses, that is, $m_\alpha = (0.3 \pm 0.3)$ m_0, $m_\beta = (0.13 \pm 0.05)$ m_0, and $m_\gamma = (0.7 \pm 0.3)$ m_0, where m_0 is the bare electron mass. Recent DFT calculations indicate that γ-MoC might display a nontrivial electronic topology, being a Dirac nodal line semimetal, which could become superconducting upon hole doping (12). The same calculations indicate that the Fermi surface should be composed of additional, larger Fermi surface sheets not detected in this study, probably because the measurements should be performed under higher fields. The associated surface states are proposed to be good candidates to host unconventional superconductivity upon doping (13).

In this work, we have established a two-step route to synthesize a TMC/TMD heterolayered material, comprising γ-MoC and MoS₂. Extensive characterization has been carried out to elucidate the structural details and the formation mechanism of the TMC/TMD vertical heterostructures. We have found that the molybdenum carbide undergoes a series of phase transitions between the α-γ′–γ phases during synthesis, which are mainly driven by nonequilibrium chemical processes that occur upon chalcogen incorporation into α-Mo₂C. The overall result leads to a highly controlled tunable superconductivity in vertical heterostructures displaying moiré patterns and other epitaxial crystallographic orders. Moreover, we can increase the T_C by 50% when compared to that of the starting material. Our structural analysis of the heterostacks reveals interfacial strain along with the emergence of the γ′ carbide phase, resulting in an increment in the frequency of the relevant phonon modes or in the electron-phonon coupling, contributing to a higher T_C. Therefore, several factors are likely to contribute to this experimental observation and further tuning of the heterostacks could be achieved and studied in the near future.

Thus, we have developed a sulfurization route for inducing strained phase transitions in metal carbide systems, alternative to the established approach of carbon incorporation (23), which provides a platform to investigate the superconducting properties of different crystallographic phases at their interfaces. Notice that α-MoC (not α-Mo₂C) was recently predicted to display a nontrivial Z_2 invariant, implying that its surface states could be harvested to induce $p + ip$ triplet superconductivity, for instance, through the use of an external gate (13). Notice that topological surface bands (drumhead states) in γ-MoC (with C termination) are predicted to lie around the Fermi level (30). Therefore, nontrivial superconducting pairing might occur in γ-MoC upon doping or gating (13). Notice that β-MoC crystallizes in the same structure as WC, corresponding to the $P\bar{6}m2$ group (or No. 187), which is predicted to display type-II triply degenerate fermions, making this compound also a good candidate for unconventional topological behavior (13). Therefore, the precise control achieved in the growth of molybdenum carbide/disulfide vertical heterostructures could open unique opportunities, not only for research in topological materials and related surface states, but also in unconventional superconductivity. Moreover, we envisage that the superconductor/semiconductor heterojunctions will play a key role in tunneling experiments, to evaluate the pairing symmetry of these compounds and resulting heterostructures through Cooper pair tunneling, as well as in functional electronic components and catalysis applications. Ultimately, our developed route for engineering the various phases of molybdenum carbide embedded in the created vertical heterostructures—including novel metastable phases—led to superconducting transitions at higher temperatures. This approach could also be applied to a broad arrange of thin films, including tungsten- and niobium-based carbides, metal nitrides, and their different stacked combinations with intriguing transport properties. We envisage that the engineering of the proposed layered heterostacks of carbides, nitrides, and sulfides of other transition metals will either introduce superconductivity in hitherto undiscovered phases, or increase the superconducting transition in known compounds.

Materials and Methods

Atmospheric-Pressure CVD Synthesis of 2D α-Mo₂C on Molten Cu. Two-dimensional Mo₂C domains were grown through atmospheric-pressure CVD directly onto Cu substrates as previously reported (11). In our experiments, Ar carrier gas with a small CH₄ flow (Ar:CH₄ = 500:1) was directed to stacked Mo/Cu metal foils which were enclosed between quartz slides, inside a quartz reaction tube at 1,090 °C. A high cooling rate (~200 °C/min) is set after 15–30 min of growth. The α-Mo₂C crystals were transferred from the Mo-Cu assembly onto arbitrary substrates, such as Si/SiO₂ or TEM grids, via a polymethyl methacrylate-assisted method by etching in an FeCl₃ solution for 3 h.

Formation of MoS₂/Carbide Heterostructures. As-grown α-Mo₂C crystals were transferred onto Si/SiO₂ (300-nm thickness) and were subjected to a heat treatment under a controlled sulfur-rich environment. The reaction was performed under a H₂S flow at a rate of 5 sccm, where ultrahigh-purity argon gas was used as a carrier gas so as to maintain a total flow rate of 35 sccm. Sulfurization was achieved at reactor pressure of ~750 mTorr for 1–20 min at 600 °C.

Materials Characterization. SEM was performed using a Zeiss Merlin FESEM at 5 kV. A Renishaw inVia microscope with a 488-nm excitation laser was used for acquiring the Raman spectra, while using a backscattering configuration, with an 1,800 line per millimeter grating. XRD patterns were acquired with a PANalytical Empryean X-Ray diffractometer equipped with a Cu source. XPS experiments were performed using a Physical Electronics VersaProbe II instrument. The binding energy axis was calibrated using sputter-cleaned Cu foil (Cu 2p₃/₂ = 932.7 eV, Cu 2p₃/₂ = 75.1 eV).

The cross-section TEM samples were prepared by FIB using an FEI SEM Helios Nanolab 660. The as-synthesized pristine Mo₂C and carbide/disulfide heterostructure flakes were initially characterized via Raman spectroscopy, XRD, SEM, and STM, followed by device fabrication (method details below) and transport measurements. Cross-sectional TEM samples of the various flakes used for transport measurements were prepared by SEM/FIB, thus all of the characterizations were conducted on the same flakes. HRTEM and STEM-EDS of the cross-section of the sample were performed with an FEI Talos F200× microscope using a SuperX EDS detector, operated at 200 kV. Aberration-corrected (S)TEM images were obtained using an FEI Titan G² 60–300 microscope, operated at 80 kV equipped with double-spherical aberration correction, offering subangstrom image resolution. An HAADF detector with a collection angle of 42–244 mrad, camera length of 115 mm, beam current of 45 pA, and beam convergence of 30 mrad was used for STEM image acquisition. For the HAADF-STEM images, a Gaussian blur filter ($r = 2.00$) was applied (by the ImageJ program) to eliminate noise and enhance the visibility of the structural details, while the line profiles of HRTEM and annular dark-field intensity were captured by analyzing raw STEM images.

STM measurements were performed at 77 K with a platinum iridium tip in a custom-built ultrahigh vacuum (UHV) STM system with an SPECS Tyto scan head. Samples were transferred to the STM vacuum chamber and annealed at 200 °C for about 2 h in a UHV environment before being loaded into the scan head for measurements, in order to eliminate any moisture absorbed on the surface. Images in Fig. 1 *A* and *B* were obtained under constant current feedback at –0.7-V bias voltage, 100-pA tunneling current and 0.4 V bias voltage, 20-pA tunneling current, respectively. STS measurements were performed using a standard lock-in technique by detecting modulation in the tunneling current in response to a bias-voltage modulation of 10 mV at 981 Hz.

DFT Calculations. The DFT calculations were performed using the plane-wave basis and projector augmented wave method (33) within the Vienna Ab initio Simulation Package (34). Before stacking MoS₂ within γ-MoC heterostructures, the pristine MoS₂ and γ-MoC were fully relaxed to reach the

energy minimum state. For converging the energy to a value within 1 meV per atom, a 600-eV cutoff energy, 20 Å of vacuum in the direction perpendicular to the MoS_2 or γ-MoC surface, and a $13 \times 13 \times 1$ k-point mesh was required. The Perdew–Burke–Ernzerhof generalized gradient functional (35) was chosen as an exchange-correlation functional.

To acquire dispersion interactions between 2D multilayers, the nonlocal vdW-DF-optB88 exchange-correlation functional (36) was employed. When the heterostructure was stacked in the strained-epitaxial case, an odd number of layers of MoS_2 was epitaxially strained to match the lattice parameter of γ-MoC, and six layers of MoC were added to obtain the γ-MoC/MoS_2/γ-MoC sandwich structure with the same termination at both interfaces. When the heterostructure was stacked in the moiré epitaxy case, the MoS_2 and γ-MoC unit cells were expanded to $10 \times 10 \times 3$ and $11 \times 11 \times 6$, respectively, to match the lattice parameter to within a 0.3% difference. The DOS and electron density map calculations were performed using the local-density approximation (LDA) functional (37). The choice of functional was determined considering the overall supercell size and bandgap value. In the moiré epitaxy case, the supercell contained over 2,200 atoms, which is beyond the capability of other more complicated functionals.

The calculated bandgap of pristine monolayer MoS_2 is 1.69 eV, which is closer to the energy of the photoluminescence experimental measurement (29) than the energies obtained from the generalized gradient approximation and the hybrid functional. Although the LDA underestimates the bandgap in semiconductors and insulators when compared with experimental results, the obtained values are reasonably accurate since the inaccuracy comes from systematic errors instead of any physical error. The DOS was analyzed in s, p, and d electron orbitals from each atomic layer in the direction perpendicular to the interface.

Superconductivity Measurement. To fabricate the electrical contacts, standard e-beam lithography and e-beam evaporation techniques were used to deposit 50 nm of Au on 5 nm of Ti. Measurements as a function of magnetic field and temperature were performed in a Physical Properties Measurement System using conventional electronics.

Data Availability. All study data are included in the article and Supporting Information.

1. Q. H. Wang, K. Kalantar-Zadeh, A. Kis, J. N. Coleman, M. S. Strano, Electronics and optoelectronics of two-dimensional transition metal dichalcogenides. *Nat. Nanotechnol.* **7**, 699–712 (2012).
2. R. Lv *et al.*, Two-dimensional transition metal dichalcogenides: Clusters, ribbons, sheets and more. *Nano Today* **10**, 559–592 (2015).
3. J.-F. Ge *et al.*, Superconductivity above 100 K in single-layer FeSe films on doped $SrTiO_3$. *Nat. Mater.* **14**, 285–289 (2015).
4. J. T. Ye *et al.*, Superconducting dome in a gate-tuned band insulator. *Science* **338**, 1193–1196 (2012).
5. X. Xi *et al.*, Ising pairing in superconducting $NbSe_2$ atomic layers. *Nat. Phys.* **12**, 139 (2016).
6. S. C. de la Barrera *et al.*, Tuning Ising superconductivity with layer and spin-orbit coupling in two-dimensional transition-metal dichalcogenides. *Nat. Commun.* **9**, 1427 (2018).
7. J. Peng *et al.*, High phase purity of large-sized 1T′-MoS_2 monolayers with 2D superconductivity. *Adv. Mater.* **31**, e1900568 (2019).
8. Y. Li *et al.*, Nontrivial superconductivity in topological $MoTe_{2-x}S_x$ crystals. *Proc. Natl. Acad. Sci. U.S.A.* **115**, 9503–9508 (2018).
9. F. Chen *et al.*, Superconductivity enhancement in the S-doped Weyl semimetal candidate $MoTe_2$. *Appl. Phys. Lett.* **108**, 162601 (2016).
10. D. Rhodes *et al.*, Enhanced superconductivity in monolayer Td-$MoTe_2$ with tilted ising spin texture. arXiv:1905.06508 (16 May 2019).
11. C. Xu *et al.*, Large-area high-quality 2D ultrathin Mo_2C superconducting crystals. *Nat. Mater.* **14**, 1135–1141 (2015).
12. A. Huang *et al.*, Multiple topological electronic phases in superconductor MoC. *Phys. Rev. Mater.* **2**, 054205 (2018).
13. G. Chang *et al.*, Nexus fermions in topological symmorphic crystalline metals. *Sci. Rep.* **7**, 1688 (2017).
14. L. Fu, C. L. Kane, Superconducting proximity effect and Majorana fermions at the surface of a topological insulator. *Phys. Rev. Lett.* **100**, 096407 (2008).
15. H. W. Hugosson *et al.*, Theory of phase stabilities and bonding mechanisms in stoichiometric and substoichiometric molybdenum carbide. *J. Appl. Phys.* **86**, 3758–3767 (1999).
16. W. Hsu *et al.*, Mixed-phase $W_xMo_yC_zS_2$ nanotubes. *Chem. Mater.* **12**, 3541–3546 (2000).
17. M. A. R. Anjum, M. H. Lee, J. S. Lee, BCN network-encapsulated multiple phases of molybdenum carbide for efficient hydrogen evolution reactions in acidic and alkaline media. *J. Mater. Chem. A* **5**, 13122–13129 (2017).
18. C. Tang *et al.*, Sulfur-decorated molybdenum carbide catalysts for enhanced hydrogen evolution. *ACS Catal.* **5**, 6956–6963 (2015).
19. T. P. St. Clair *et al.*, Surface characterization of α-Mo_2C (0001). *Surf. Sci.* **426**, 187–198 (1999).
20. D. Geng *et al.*, Direct synthesis of large-area 2D Mo_2 C on in situ grown graphene. *Adv. Mater.* **29**, 1700072 (2017).
21. Z. Liu *et al.*, Phase transition and in situ construction of lateral heterostructure of 2D superconducting α/β Mo_2C with sharp interface by electron beam irradiation. *Nanoscale* **9**, 7501–7507 (2017).
22. T. Y. Velikanova, V. Kublii, B. Khaenko, Solid state transformations and phase equilibria in the molybdenum-carbon system. *Sov. Powder Metall. Met. Ceram.* **27**, 891–896 (1988).
23. J. Lu, H. Hugosson, O. Eriksson, L. Nordström, U. Jansson, Chemical vapour deposition of molybdenum carbides: Aspects of phase stability. *Thin Solid Films* **370**, 203–212 (2000).
24. N. Morton *et al.*, Superconductivity of molybdenum and tungsten carbides. *J. Less Common Met.* **25**, 97–106 (1971).
25. W. Meissner, H. Franz, Messungen mit Hilfe von flüssigem Helium. IX. Supraleitfähigkeit von Carbiden und Nitriden. *Z. Phys.* **65**, 30–54 (1930).
26. F. Zhang *et al.*, Controlled synthesis of 2D transition metal dichalcogenides: from vertical to planar MoS_2. *2D Mater.* **4**, 025029 (2017).
27. G. Z. Cambaz, G. N. Yushin, Y. Gogotsi, V. G. Lutsenko, Anisotropic etching of SiC whiskers. *Nano Lett.* **6**, 548–551 (2006).
28. R. A. Klemm, Pristine and intercalated transition metal dichalcogenide superconductors. *Physica C* **514**, 86–94 (2015).
29. K. F. Mak, C. Lee, J. Hone, J. Shan, T. F. Heinz, Atomically thin MoS_2: A new direct-gap semiconductor. *Phys. Rev. Lett.* **105**, 136805 (2010).
30. S. Hikami, A. I. Larkin, Y. Nagaoka, Spin-orbit interaction and magnetoresistance in the two dimensional random system. *Prog. Theor. Phys.* **63**, 707–710 (1980).
31. D. Shoenberg, *Magnetic Oscillations in Metals*, (Cambridge Monographs on Physics, Cambridge University Press, 1984).
32. N. Armitage, E. Mele, A. Vishwanath, Weyl and Dirac semimetals in three-dimensional solids. *Rev. Mod. Phys.* **90**, 015001 (2018).
33. P. E. Blöchl, Projector augmented-wave method. *Phys. Rev. B Condens. Matter* **50**, 17953–17979 (1994).
34. G. Kresse, J. Furthmüller, Efficient iterative schemes for ab initio total-energy calculations using a plane-wave basis set. *Phys. Rev. B Condens. Matter* **54**, 11169–11186 (1996).
35. J. P. Perdew, K. Burke, M. Ernzerhof, Generalized gradient approximation made simple. *Phys. Rev. Lett.* **77**, 3865–3868 (1996).
36. M. Dion, H. Rydberg, E. Schröder, D. C. Langreth, B. I. Lundqvist, van der Waals density functional for general geometries. *Phys. Rev. Lett.* **92**, 246401 (2004).
37. A. D. Becke, Completely numerical calculations on diatomic molecules in the local-density approximation. *Phys. Rev. A Gen. Phys.* **33**, 2786–2788 (1986).